

Electronic transition above room temperature in $\text{CaMn}_7\text{O}_{12}$ films

A. Huon,¹ A. C. Lang,¹ D. Saldana-Greco,² J. S. Lim,² E. J. Moon,¹ A. M. Rappe,²
 M. L. Taheri,¹ and S. J. May^{1,a)}

¹Department of Materials Science and Engineering, Drexel University, Philadelphia, Pennsylvania 19104, USA

²The Makineni Theoretical Laboratories, Department of Chemistry, University of Pennsylvania, Philadelphia, Pennsylvania 19104-6323, USA

(Received 28 July 2015; accepted 18 September 2015; published online 5 October 2015)

We report on the electronic phase transition in $\text{CaMn}_7\text{O}_{12}$ quadruple perovskite films synthesized by oxide molecular beam epitaxy on SrLaAlO_4 and $\text{La}_{0.3}\text{Sr}_{0.7}\text{Al}_{0.65}\text{Ta}_{0.35}\text{O}_3$ substrates. We use x-ray diffraction and transmission electron microscopy to confirm that the $\text{CaMn}_7\text{O}_{12}$ phase has been realized. Temperature dependent resistivity measurements reveal a signature of a charge ordering phase transition at ≈ 425 K, consistent with bulk $\text{CaMn}_7\text{O}_{12}$. The transition temperature is found to be relatively invariant to changes in the cation stoichiometry. Density functional theory calculations reveal the changes in atomic and electronic structure induced by the charge ordering transition. © 2015 AIP Publishing LLC. [<http://dx.doi.org/10.1063/1.4932132>]

Complex oxides that exhibit electronic phase transitions are of interest both to the fundamental scientific understanding of electronic structure in solids and their potential application in next generation electronics.^{1–8} Charge ordering transitions are a promising platform for devices, as these transitions often result in abrupt changes in resistivity and occur at ultrafast time scales.^{9–12} However, the charge ordering transition temperature (T^*) observed in many ABO_3 perovskites is below room temperature, motivating a need to identify, understand, and design new high T^* materials. One candidate material is $\text{CaMn}_7\text{O}_{12}$, which is a quadruple perovskite in which 3/4 and 1/4 of the A-sites are occupied by Mn and Ca, respectively, with the Mn and Ca ordering on the A-site.^{13,14} Previous studies of $\text{CaMn}_7\text{O}_{12}$ have provided evidence for a charge ordering transition near 440 K that is accompanied by an abrupt change in resistivity and a concurrent structural change from a distorted cubic ($Im\bar{3}$) to a rhombohedral ($R\bar{3}$) structure.¹⁵ The charge ordering in $\text{CaMn}_7\text{O}_{12}$ occurs on the B-site Mn cations, with 3/4 taking on a nominal 3+ valence and 1/4 exhibiting a 4+ valence, as evidenced by structural distortions of the MnO_6 octahedra measured by powder diffraction.¹⁶ In addition to the coupled charge ordering/structural transition, $\text{CaMn}_7\text{O}_{12}$ exhibits an orbital ordering transition at 250 K and two magnetic transitions at 90 K (T_{N1}) and 45 K (T_{N2}) that correspond to the onset of helical magnetic states characterized by one and two propagation vectors below T_{N1} and T_{N2} , respectively.^{15,17–19} The non-collinear magnetic ordering breaks inversion symmetry inducing ferroelectricity, with one of the largest magnetically induced polarizations yet reported.^{20,21}

These previous works have revealed rich physics in bulk $\text{CaMn}_7\text{O}_{12}$ samples, with particular emphasis on the low temperature properties. However, there have yet to be reports of $\text{CaMn}_7\text{O}_{12}$ films, which are the material architecture of interest for device applications. Additionally, a detailed understanding of how the electronic structure is altered across the high temperature charge ordering transition is lacking. In

this work, we synthesize $\text{CaMn}_7\text{O}_{12}$ thin films using oxide molecular beam epitaxy (MBE) and use x-ray diffraction (XRD) and transmission electron microscopy (TEM) to confirm the films are phase pure and have lattice parameters in agreement with bulk $\text{CaMn}_7\text{O}_{12}$. A change in resistivity near 425 K is observed, consistent with the charge ordering transition previously reported. Density functional theory (DFT) is used to elucidate the changes to the electronic structure across the phase transition, including the opening of a small band gap below T^* .

The $\text{CaMn}_7\text{O}_{12}$ films were deposited on single crystalline (001) SrLaAlO_4 (SLAO) and $\text{La}_{0.3}\text{Sr}_{0.7}\text{Al}_{0.65}\text{Ta}_{0.35}\text{O}_3$ (LSAT) substrates using oxide MBE. The lattice mismatch between these substrates and $\text{CaMn}_7\text{O}_{12}$ is 2.0% and 5.1% for SLAO and LSAT, respectively. The film thicknesses are 50–60 nm. Deposition was carried out in an O_2 environment at a chamber pressure of 2×10^{-6} Torr with Ca and Mn co-evaporated from Knudsen cells with a 10 s pause following the deposition of each unit cell. Typical substrate temperatures ranged from 600 to 700 °C for deposition. Post-growth anneals were carried out in an oxygen tube furnace following a two-step annealing process consisting of 2–3 h at 850 °C under flowing O_2 followed by 1 h at 200 °C under a flowing 95:5 O_2/O_3 mixture.²² The high temperature of 850 °C was chosen based on previously reported bulk synthesis conditions.²³ The post-growth anneal step was critical to stabilizing the correct phase, as described in the supplementary material.²⁴ Using Rutherford backscattering spectrometry (RBS), cation stoichiometry was measured on as-grown films deposited on MgO that were grown simultaneously to the films on SLAO and LSAT; the SIMNRA software package was used to simulate and analyze the RBS data. Samples from three depositions are reported in this work. The Mn:Ca ratios measured from films on MgO for samples A, B, and C are 6.8, 7.0, and 7.3, respectively. However, we note that differences in sticking coefficient or position on the sample mount within the growth chamber could lead to slight variations in the cation composition between the films on MgO, SLAO, and LSAT. XRD and x-ray reflectivity (XRR) were

^{a)}Electronic mail: smay@coe.drexel.edu

JEOL specified 2100 LaB₆ optics, for a sample approximately 35 nm thick with a defocus set to 45.6 nm. Selected area diffraction patterns from films grown on SLAO and LSAT are shown in Figures 2(a) and 2(b), respectively. They show highly textured films with well-defined film reflections; the measured *c*-axis parameter of 3.68 Å is consistent with our XRD results. All measured diffraction spots can be indexed to the film or substrate. Low resolution TEM images shown in Figures 2(c) and 2(d) reveal the typical morphology of the CaMn₇O₁₂ films. The film/substrate interface is marked by defects, and while the film contains many grains, they are highly textured with only a slight misorientation between grains. Filtered HRTEM images shown in Figures 2(e) and 2(f) reveal the periodic structure of the CaMn₇O₁₂ films; for visual clarity, a structural cartoon of CaMn₇O₁₂ (without O atoms present) in the [100] pseudocubic orientation is superimposed over Figure 2(f). The most notable feature in the HRTEM images is the spacing between atomic columns, approximately 5.4 Å, which is consistent with the expected *A*-site ordering, the Ca-Ca distance, of this structure when projected in two dimensions due to the orientation of the sample. Further evidence for the *A*-site ordering of Ca and Mn cations is found in the presence of (0 1/2 1/2) reflections, in the pseudocubic notation, in the selected area diffraction patterns.

Evidence for the charge ordering phase transition in CaMn₇O₁₂ films was obtained using temperature dependent resistivity (ρ) measurements, displayed in Figure 3. The CaMn₇O₁₂ films exhibit an abrupt change in resistivity near 425 K. These results are consistent with previous resistivity measurements on bulk CaMn₇O₁₂, suggesting the resistivity feature is due to charge ordering.¹⁵ The results are reproducible after repeated temperature cycling in air up to 600 K, indicating that the films are not susceptible to low temperature oxygen loss as has been observed in some other systems with charge ordering transitions.⁴¹ Additionally, we note that the magnitude of resistivity is consistent with bulk CaMn₇O₁₂; for the films, $\rho_{300\text{K}} = 3\text{--}100 \text{ } \Omega \text{ cm}$, while for bulk CaMn₇O₁₂, $\rho_{300\text{K}} = 10\text{--}535 \text{ } \Omega \text{ cm}$ has been reported.^{15,42} As can be seen in Figure 3(a), slight variations in cation stoichiometry do not significantly alter the phase transition. To determine the transition temperature (T^*), we fit $d(\ln\rho)/dT$ as a function of T to a bi-gaussian function; the center position is taken as T^* , as detailed in the supplementary material.²⁴ For the films A, B, and C on SLAO, T^* is 429 K, 420 K, and 426 K, respectively. For comparison, applying this analysis to the data reported in Ref. 15 for bulk CaMn₇O₁₂ yields a T^* of 434 K. As shown in Figure 3(b), the general features of the phase transition are similar for the films grown on SLAO and LSAT, despite the larger resistivity observed in the films on LSAT.

The temperature dependent resistivity was analyzed within the context of various models to gain further insight into the nature of electronic transport above (450–600 K) and below ($\approx 175\text{--}300 \text{ K}$) the transition. At temperatures above T^* , we find that models for polaron transport yield the highest R^2 values, although activated behavior also yields R^2 values greater than 0.999. Activation energies obtained from fits to adiabatic and non-adiabatic polaron models range from 190 to 220 meV and 210 to 240 meV, respectively. The fits

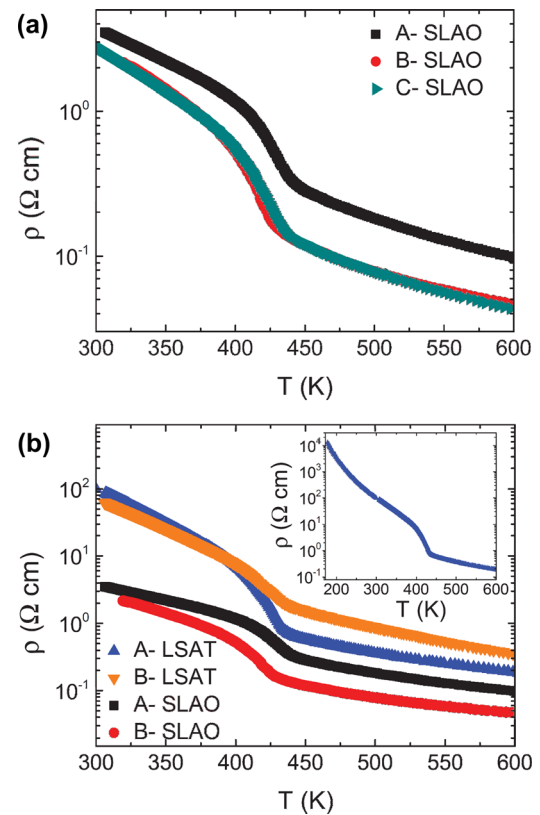


FIG. 3. Temperature dependent resistivity of CaMn₇O₁₂ films reveals signatures of a charge ordering transition near 425 K. For films grown on SLAO (a), slight variations in Mn:Ca ratio have minimal effect on T^* . Similarly, films grown on LSAT are more resistive than compositionally equivalent films on SLAO (b), but the change in substrate does not significantly alter T^* . The resistivity of sample A-LSAT measured over a wider temperature range is shown as an inset of (b).

to adiabatic and non-adiabatic models are comparable, preventing us from distinguishing which model is more appropriate based on our data. Below T^* , activated transport provides the highest R^2 values. The activation energies obtained from the Arrhenius plots are approximately 100 meV for the films on SLAO and 180 meV for the films on LSAT. These activation energies are consistent with the 180 meV activation energy previously reported for bulk CaMn₇O₁₂.²³ Complete details of the fitting, including R^2 values and activation energies for all samples, can be found in the supplementary material.²⁴

Important insights into the atomistic and electronic structure properties of the charge ordering phase transition are provided by first-principles DFT calculations. Our simulations explore the coupled structural and electronic phase transition that occurs through the crystal symmetry lowering process from a metallic state crystallized with space group $Im\bar{3}$ to an insulating $R\bar{3}$ state. This phase transition lowers the energy of the system by 52 meV indicating the insulating $R\bar{3}$ structure as the ground state. The relaxed atomic structures are illustrated in Figures 4(a) and 4(b), respectively, with *A*-site Mn denoted as Mn1 and *B*-site Mn denoted as Mn2 and Mn3. These structural changes are activated by electron-electron interactions between the *B*-site Mn 3*d* and O 2*p* orbitals as the charge is localized in an orderly fashion throughout the Mn-sites. A collective shortening and elongation of Mn-O bond lengths then leads to significant

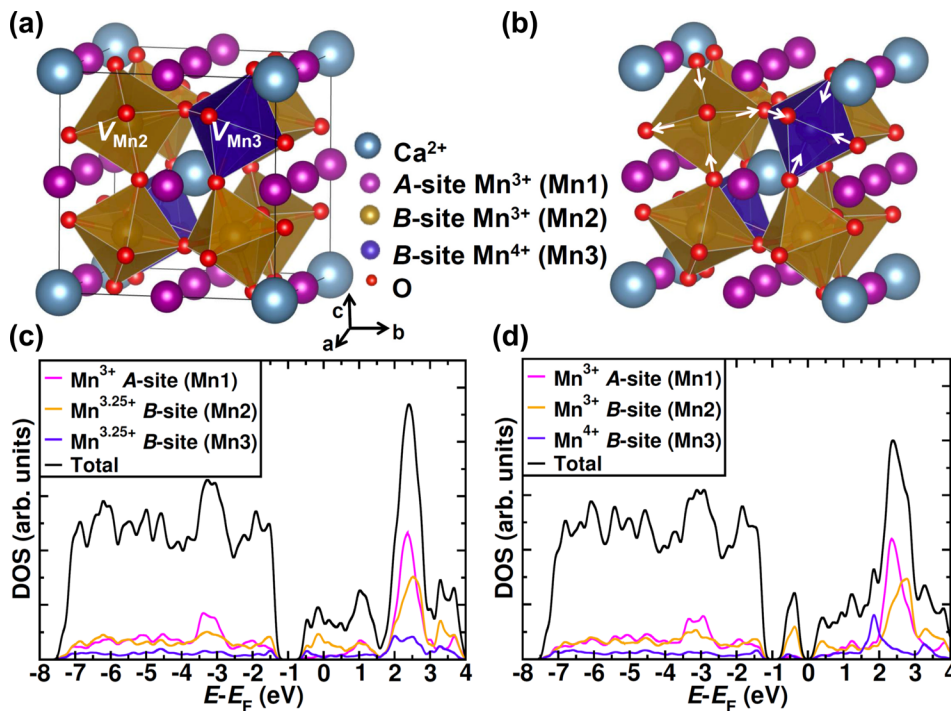


FIG. 4. Crystal and electronic structure of $\text{CaMn}_7\text{O}_{12}$. (a) Distorted cubic structure, $Im\bar{3}$, where the Mn_2O_6 and Mn_3O_6 octahedral volumes are nearly identical, $V_{\text{Mn}2} \approx V_{\text{Mn}3}$. (b) Lowest energy rhombohedral structure, $R\bar{3}$, where $V_{\text{Mn}2} > V_{\text{Mn}3}$, suggesting a charge-ordered atomic structure. Both structures in (a) and (b) display the pseudocubic direction for simplicity; the white arrows indicate the shortening and elongation of Mn-O bonds lengths that lead to the changes in the octahedral volume. (c) Projected density of states of the distorted cubic structure in (a) showing a metallic state, where the *B*-site Mn2 and Mn3 nominally have a 3.25+ valence. (d) Projected density of states of the rhombohedral structure in (b) showing an insulating state with a ≈ 240 meV band gap, where the *B*-site Mn2 and Mn3 have 3+ and 4+ valences, respectively.

differences in the MnO_6 octahedral cage volumes. In the high-temperature $Im\bar{3}$ structure, all *B*-site Mn-O bond lengths are identical as are the octahedral cage volumes.

The projected density of states of the $Im\bar{3}$ system, shown in Figure 4(c), reveals states around the Fermi level, and both Mn2 and Mn3 states are very similar. This suggests that all *B*-site Mn ions have the same charge density leading to a metallic system, as there is free flow of electrons through the Mn-O bonds, which could be thought of as one electron shared by every four Mn atoms, for a fractional charge of 3.25+. Below the phase transition temperature in the $R\bar{3}$ structure, the charge is localized along the $[111]$, generating charge balance with three Mn^{3+} (Mn2) per every Mn^{4+} (Mn3). The Mn_3O_6 octahedral volume decreases as a consequence of shorter and equal Mn3-O bonds. This is typical of Mn3 electronic structure, which consists of $3d^3$ with half filled t_{2g} shells and empty e_g shells. The Mn_2O_6 octahedral volume increases, since four Mn2-O bonds elongate due to Jahn-Teller interactions. This is due to the electronic structure of Mn2 (consisting of $3d^4$). The Jahn-Teller distortions break the degenerate e_g into $d_{x^2-y^2}$, d_{z^2} and t_{2g} into d_{xy} , (d_{xz}, d_{yz}) . The electronic structure of the charge-ordered state, shown in Fig. 4(d), exhibits an electronic gap of 240 meV, where both the valence and conduction band edges are composed of Mn 3d and O 2p orbitals. The changes in the electronic structure couple to the atomic structural distortions as the octahedral volumes vary from equal volume, $V_{\text{Mn}2} \approx V_{\text{Mn}3}$, to $V_{\text{Mn}2} = V_{\text{Mn}3} + 1.15 \text{ \AA}^3$.

The calculated band structures are also useful in differentiating between the applicable transport mechanisms. Below T^* , the resistivity is best described by an activated model consistent with the small band gap obtained from the first principles calculations. Above T^* , the DFT calculations reveal a metallic band structure, which can be reconciled with the observed semiconductor-like transport behavior if polaronic conduction is dominant, as supported by the

resistivity analysis. We note that polaronic conduction is commonly observed at high temperatures in nominally metallic manganites such as $\text{La}_{0.7}\text{Ca}_{0.3}\text{MnO}_3$, with activation energies on the order of 70–200 meV.^{43–45}

We have carried out a combined theoretical and experimental study of $\text{CaMn}_7\text{O}_{12}$ films. We have synthesized $\text{CaMn}_7\text{O}_{12}$ in thin film form, as indicated by RBS, XRD, and TEM characterization. Temperature dependent resistivity measurements confirm the presence of an electronic transition near 425 K. DFT simulations elucidate changes in the electronic structure due to the charge ordering transition, most importantly the opening of a band gap below T^* . The synthesis of $\text{CaMn}_7\text{O}_{12}$ thin films is a step toward room temperature devices based on charge ordering transitions and enables future studies of the effects of biaxial strain, thickness effects, and interfacial proximity on $\text{CaMn}_7\text{O}_{12}$.

We thank Boris Yakshinskiy for RBS measurements at the Rutgers University Laboratory for Surface Modification. We also thank Jenia Karapetrova and Rebecca Sichel-Tissot for measurement of the reciprocal space maps. A.H., A.C.L., D.S.G., M.L.T., and S.J.M. were supported by the U.S. Office of Naval Research, under Grant No. N00014-11-1-0664. J.S.L. wishes to thank the Vagelos Integrated Program in Energy Research (VIPER) at the University of Pennsylvania. A.M.R. was supported by the U.S. Department of Energy, under Grant No. DE-FG02-07ER46431. E.J.M. acknowledges support from the U.S. Army Research Office, under Grant No. W911NF-15-1-0133. The authors acknowledge computational support from the High-Performance Computing Modernization Office (HPCMO) of the U.S. Department of Defense, as well as the National Energy Research Scientific Computing (NERSC) center. Acquisition of the PPMS was supported by the U.S. Army Research Office under Grant No. W911NF-11-1-0283. The x-ray diffractometer was acquired with funds from NSF MRI Award No. DMR-1040166.

- ¹M. Imada, A. Fujimori, and Y. Tokura, *Rev. Mod. Phys.* **70**, 1039 (1998).
- ²I. I. Mazin, D. I. Khomskii, R. Lengsdorf, J. A. Alonso, W. G. Marshall, R. M. Ibberson, A. Podlesnyak, M. J. Martinez-Lope, and M. M. Abd-Elmeguid, *Phys. Rev. Lett.* **98**, 176406 (2007).
- ³A. Cammarata and J. M. Rondinelli, *Phys. Rev. B* **86**, 195144 (2012).
- ⁴H. Park, A. J. Millis, and C. A. Marianetti, *Phys. Rev. Lett.* **109**, 156402 (2012).
- ⁵W. E. Pickett, Y. Quan, and V. Pardo, *J. Phys.: Condens. Matter* **26**, 274203 (2014).
- ⁶L. Jiang, D. Saldana-Greco, J. T. Schick, and A. M. Rappe, *Phys. Rev. B* **89**, 235106 (2014).
- ⁷Z. Yang, C. Ko, and S. Ramanathan, *Annu. Rev. Mater. Res.* **41**, 337 (2011).
- ⁸N. Shukla, A. Parihar, E. Freeman, H. Paik, G. Stone, V. Narayanan, H. Wen, Z. Cai, V. Gopalan, R. Engel-Herbert, D. G. Schlom, A. Raychowdhury, and S. Datta, *Sci. Rep.* **4**, 4964 (2014).
- ⁹Y. Tomioka, A. Asamitsu, H. Kuwahara, Y. Moritomo, and Y. Tokura, *Phys. Rev. B* **53**, R1689 (1996).
- ¹⁰A. Asamitsu, Y. Tomioka, H. Kuwahara, and Y. Tokura, *Nature* **388**, 50 (1997).
- ¹¹U. Staub, G. I. Meijer, F. Fauth, R. Allenspach, J. G. Bednorz, J. Karpinski, S. M. Kazakov, L. Paolasini, and F. d'Acapito, *Phys. Rev. Lett.* **88**, 126402 (2002).
- ¹²H. Matsuzaki, H. Uemura, M. Matsubara, T. Kimura, Y. Tokura, and H. Okamoto, *Phys. Rev. B* **79**, 235131 (2009).
- ¹³B. Bochu, J. Chenavas, J. C. Joubert, and M. Marezio, *J. Solid State Chem.* **11**, 88 (1974).
- ¹⁴A. N. Vasil'ev and O. S. Volkova, *Low Temp. Phys.* **33**, 895 (2007).
- ¹⁵I. O. Troyanchuk, L. S. Lobanovsky, N. V. Kasper, M. Hervieu, A. Maignan, and C. Michel, *Phys. Rev. B* **58**, 14903 (1998).
- ¹⁶R. Przenioslo, I. Sosnowska, E. Suard, A. Hewat, and A. N. Fitch, *J. Phys.: Condens. Matter* **14**, 5747 (2002).
- ¹⁷R. Przenioslo, I. Sosnowska, D. Hohlwein, T. Hau, and I. O. Troyanchuk, *Solid State Commun.* **111**, 687 (1999).
- ¹⁸F. Kadlec, V. Goian, C. Kadlec, M. Kempa, P. Vanek, J. Taylor, S. Rols, J. Prokleska, M. Orlita, and S. Kamba, *Phys. Rev. B* **90**, 054307 (2014).
- ¹⁹X. Du, R. Yuan, L. Duan, C. Wang, Y. Hu, and Y. Li, *Phys. Rev. B* **90**, 104414 (2014).
- ²⁰R. D. Johnson, L. C. Chapon, D. D. Khalyavin, P. Manuel, P. G. Radaelli, and C. Martin, *Phys. Rev. Lett.* **108**, 067201 (2012).
- ²¹N. J. Perks, R. D. Johnson, C. Martin, L. C. Chapon, and P. G. Radaelli, *Nat. Commun.* **3**, 1277 (2012).
- ²²Y. J. Xie, M. D. Scafetta, E. J. Moon, A. L. Krick, R. J. Sichel-Tissot, and S. J. May, *Appl. Phys. Lett.* **105**, 062110 (2014).
- ²³E. A. Pomerantseva, D. M. Itkis, E. A. Goodilin, J. G. Noudem, M. V. Lobanov, M. Greenblatt, and Yu. D. Tretyakov, *J. Mater. Chem.* **14**, 1150 (2004).
- ²⁴See supplementary material at <http://dx.doi.org/10.1063/1.4932132> for additional data and analysis of the x-ray diffraction, transmission electron microscopy, electronic transport, and the atomic structures obtained from DFT.
- ²⁵M. Bjorck and G. Andersson, *J. Appl. Crystallogr.* **40**, 1174 (2007).
- ²⁶J. P. Perdew, A. Ruzsinszky, G. I. Csonka, O. A. Vydrov, G. E. Scuseria, L. A. Constantin, X. Zhou, and K. Burke, *Phys. Rev. Lett.* **100**, 136406 (2008).
- ²⁷B. Himmetoglu, R. M. Wentzcovitch, and M. Cococcioni, *Phys. Rev. B* **84**, 115108 (2011).
- ²⁸P. Giannozzi, S. Baroni, N. Bonini, M. Calandra, R. Car, C. Cavazzoni, D. Ceresoli, G. L. Chiarotti, M. Cococcioni, I. Dabo, A. Dal Corso, S. de Gironcoli, S. Fabris, G. Fratesi, R. Gebauer, U. Gerstmann, C. Gougousis, A. Kokalj, M. Lazzeri, L. Martin-Samos, N. Marzari, F. Mauri, R. Mazzarello, S. Paolini, A. Pasquarello, L. Paulatto, C. Sbraccia, S. Scandolo, G. Sclauzero, A. P. Seitsonen, A. Smogunov, P. Umari, and R. M. Wentzcovitch, *J. Phys.: Condens. Matter* **21**, 395502 (2009).
- ²⁹X. Z. Lu, M.-H. Whangbo, S. Dong, X. G. Gong, and H. J. Xiang, *Phys. Rev. Lett.* **108**, 187204 (2012).
- ³⁰E. Bousquet and N. Spaldin, *Phys. Rev. B* **82**, 220402 (2010).
- ³¹A. M. Rappe, K. M. Rabe, E. Kaxiras, and J. D. Joannopoulos, *Phys. Rev. B* **41**, 1227 (1990).
- ³²N. J. Ramer and A. M. Rappe, *Phys. Rev. B* **59**, 12471 (1999).
- ³³See <http://opium.sourceforge.net> for information on the Opium software package.
- ³⁴G. Theurich and N. A. Hill, *Phys. Rev. B* **64**, 073106 (2001).
- ³⁵M. Fuchs and M. Scheffler, *Comput. Phys. Commun.* **119**, 67 (1999).
- ³⁶D. Porezag, M. R. Pederson, and A. Y. Liu, *Phys. Rev. B* **60**, 14132 (1999).
- ³⁷H. J. Monkhorst and J. D. Pack, *Phys. Rev. B* **13**, 5188 (1976).
- ³⁸W. Sławiński, R. Przenioslo, I. Sosnowska, and M. Bieringer, *J. Phys.: Condens. Matter* **22**, 186001 (2010).
- ³⁹R. M. Langford and M. Rogers, *Micron* **39**, 1325 (2008).
- ⁴⁰P. A. Stadelmann, "Electron Microscopy Software Java Version 4," see <http://cimewwww.epfl.ch/people/stadelmann/jemsWebSite/jems.html> (2015).
- ⁴¹Y. Xie, M. D. Scafetta, R. J. Sichel-Tissot, E. J. Moon, R. C. Devlin, H. Wu, A. L. Krick, and S. J. May, *Adv. Mater.* **26**, 1434 (2014).
- ⁴²Z. Zeng, M. Greenblatt, J. E. Sunstrom, M. Croft, and S. Khalid, *J. Solid State Chem.* **147**, 185 (1999).
- ⁴³M. Jaime, H. T. Hardner, M. B. Salamon, M. Rubinstein, P. Dorsey, and D. Emin, *Phys. Rev. Lett.* **78**, 951 (1997).
- ⁴⁴M. Ziese and C. Srinithiwarawong, *Phys. Rev. B* **58**, 11519 (1998).
- ⁴⁵P. Graziosi, A. Gambardella, M. Prezioso, A. Riminucci, I. Bergenti, N. Homonnay, G. Schmidt, D. Pullini, and D. Busquets-Mataix, *Phys. Rev. B* **89**, 214411 (2014).